Investigation of turbulent boundary layer flow over a circular cavity using large-eddy simulations.

Arpiruk Hokpunna[1*] and Michael Manhart[2]

[1] Department of Numerical Mathematics for Supercomputers, Stuttgart University, Stuttgart, Germany 71083

[2] Department of Hydromechanics, Munich University of Technology, Munich, Germany 80290

* Corresponding Author: Tel: (49711) 68565883, Fax: (49711) 68565507,

E-mail: hokpunna@ians.uni-stuttgart.de

Abstract

We present a Large-Eddy simulation of a vortex cell with circular shaped. The results show that the flow field can be sub divided into four important zones, the shear layer above the cavity, the stagnation zone, the vortex core in the cavity and the boundary layer along the wall of the cavity. It is shown that the vortex core consists of solid body rotation without much turbulence activity. The vortex is mainly driven by high energy packets that are driven into the cavity from the stagnation point region and by entrainment of fluid from the cavity into the shear layer. The physics in the boundary layer along the cavity's wall seems to be far from that of a canonical boundary layer which might be a crucial point for modelling this flow.

1. Introduction

Lift enhancement and drag reduction is one of the most demanding technologies in aviation industry. To ensure a high lift-to-drag ratio, wings of modern aircraft are thin and streamlined. However, from a structural-strength point of view, having thick wings would be beneficial in order to carry a larger load. As the progress in aviation leads to an increase in the size of transport aircraft, the balance between structural-strength and aerodynamic quality shifts in favour of a thick wing. The flow past a thick airfoil, however, is likely to separate, which affects the aerodynamic performance of the wing (Fig.1a). Trapping vortices by a so-called vortex cell is considered to be able to prevent flow separation and large-scale vortex shedding which would in turn reduce the drag (Fig.1b). In this paper we investigate the physics of vortex cell flows by means of a large-eddy simulation. We consider the geometry of a round cavity as sketched in Fig.2. Significant mechanisms are identified and the study shows that this vortex cell works against flow separation mechanisms.

Control algorithms must be robust and fast, thus solving three-dimensional problems are

not allowed. An insightful understanding of the physics in vortex cell flows is required to create a two-dimensional turbulence model that is sufficiently accurate and affordable in real-time control. In order to achieve this aim, Large-Eddy simulation (LES) is the only viable option that can represent the highly transient and three dimensional nature of the problem at sufficient accuracy within affordable time. As a part of the investigation of vortex cell flows, we study a vortex cell flow with homogeneous spanwise direction. This will serve as the two-dimensional limit where LES and numerical simulation of Reynolds-Averaged Navier-Stokes equations (RANS) should agree, when the turbulence is modelled correctly. In a later phase of the study, effects of finite span and oblique direction of incoming flow can be identified using this simulation as a reference. In this work, an Investigation of the flow physics inside the vortex cell with circular shape by means of large-eddy simulation is presented. We first outline the governing equations, methodology and setup of the numerical experiment. First- and second-order statistics obtained from the numerical simulation are then presented and discussed.

<div align="center">(a)   (b)</div>
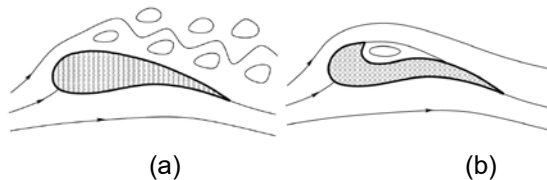
Fig.1: Flow past thick wing: (a) without trapped vortex cell and (b) with a trapped vortex cell

2. Numerical Approach

In this numerical simulation, we solve the Navier-Stokes equations for incompressible Newtonian flows:

$$\frac{\partial u}{\partial x_i} = 0 \qquad (1)$$

$$\frac{\partial u_i}{\partial t} + \frac{\partial u_j u_i}{\partial x_j} = \nu \frac{\partial^2 u_i}{\partial x_i^2} - \frac{1}{\rho} \frac{\partial p}{\partial x_i} \qquad (2)$$

The Navier-Stokes equations (NSE) are integrated within the standard framework of finite volumes using staggered Cartesian grids. The spatial approximations are second order accurate and use centered interpolations and differentiations. Time integration is performed via a fractional step method using a third-order Runge-Kutta scheme. The pressure is obtained by a projection formulation at the end of each substep. The Poisson equation is solved by Stone's strongly implicit procedure (SIP). See e.g. Ferziger and Peric [1] for a review on these standard methods. Detail information and accuracy of the code can be found in [2,3,4,5].

2.1 Immersed Boundary Method

Solid surfaces that are not ligned with the boundary of the Cartesian control volumes are represented by Immersed boundary method. The basic concept of our immersed boundary method (IBM) is a functional fitting. A certain approximated function f(x,y,z) is assumed to represent the velocity field and boundary condition locally near the interpolating point. This function is determined by the method of undetermined coefficients. Once the approximated function is obtained, velocity components at a given point can be extracted. Lagrange polynomial, cubic spline and least square polynomial are available in our code. This gives a second-order smooth representation of the curved surface in our Cartesian grid. Detail information about the immersed boundary method

can be found in [6]. The IBM used in the code has been used successfully in turbulent flows investigation [7,8,9].

2.2. Large-eddy simulation and SGS model

The computational cost of Direct Numerical Simulations (DNS) is hardly feasible for complex flows at high Reynolds number such as the vortex cell flow we intend to study. Therefore LES is the only possibility to investigate this type of flow. LES is based on the assumption that the quantities describing the turbulent flow can be decomposed into large scales and small scales. The large scales contain most of the energy and most of the flow dynamics. However, the large scales interact with the small scales and evolve in time. Therefore the small scales cannot be neglected even if we are only interested in the large scales. The goal of LES is to accurately compute the large flow structures and model the effect of the small scales together with their interaction with the large scale structure. The large scale structures are determined by a spatial filtering operation. The effect caused by the small scale structures is modelled by the subgrid stress tensor (SGS). The filtered NSE are defined as :

$$\frac{\partial \overline{u}}{\partial x_i} = 0 \qquad (3)$$

$$\frac{\partial \overline{u}_i}{\partial t} + u \frac{\partial \overline{u_i u_i}}{\partial x_j} = \nu \frac{\partial^2 \overline{u}_i}{\partial x_i^2} - \frac{1}{\rho} \frac{\partial \overline{p}}{\partial x_i} \qquad (4)$$

When the filtered NSE are solved numerically, only the filtered quantities are available. Therefore the nonlinear convective term in the above equation must be approximated. In this work we approximate it by $\overline{u_j u_i} = \overline{u}_j \overline{u}_i + \tau_{ij}$. The subgrid stress tensor τ_{ij} in this simulation is modelled by the Lagrangian dynamics SGS model of Meneveau[10] in which the average of the

Germano identity and error are minimised over the fluid particle trajectories.

3. Setup of the simulation

The shape of the cavity is shown in Fig.2. The reference length is the cavity diameter, D. A flat plate is attached to both ends of the cavity surface. The computational box is given by [Lx,Ly,Lz] = [6D,2D,5D] in streamwise, spanwise and wall normal direction, respectively. The origin of the coordinate system is located at the cavity leading edge (cusp, depicted as "D"). The turbulent inflow boundary condition is set at x=-2.85D. A block structured Cartesian grid is used to represent the flow domain. This consists of a sub domain covering the channel above the cavity and one covering the cavity only.
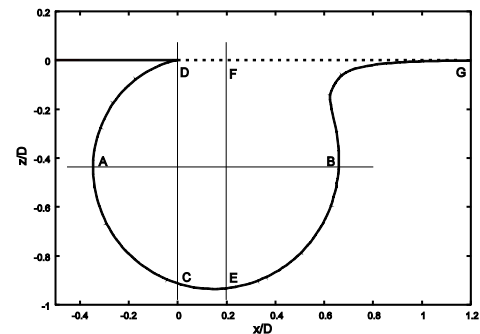

Fig 2: Cavity cell and lines of interest.

A zero-gradient velocity and zero (total) pressure is imposed at the outflow plane to which the grid is highly compressed in order to reduce numerical wiggles. A slip condition is imposed at the top wall at z=4D. The bottom boundary condition is given by the no-slip walls of the cavity. The time-dependent turbulent boundary layer at the inflow plane is constructed by a superposition of fluctuations onto a time-averaged velocity profile. In this work, a precursor simulation of canonical turbulent boundary layer is simulated using the inflow taken from DNS calculations of

Spalart[11] the fluctuations are extracted at x/δ_0 =10 downstream of the inlet by computing the difference between the instantaneous velocity and the one which was averaged in the spanwise direction. This method has proven to be useful in previous direct numerical simulations of turbulent boundary layers [12] and shown to be equivalent to the one proposed by Lund [13]. After the mean streamwise velocity adapted to the flow conditions and reached the self-similar profile, it is extracted and used as the mean inflow conditions in the present work. The boundary condition at the inflow based on boundary layer thickness is set to $\mathrm{Re}_\delta = 24,000$ where the boundary layer thickness δ is chosen to be a quarter of the cavity's diameter. The mean inflow profile and the resulting fluctuations at the inflow due to turbulence generated by the recycling of perturbations are shown in Fig.3.

The grid resolution is set to [Nx,Ny,Nz] = [564,80,145] in the channel and [Nx,Ny,Nz] = [240,80,154] in the cavity grid which add up to $9.5 \cdot 10^6$ grid cells. At their interface, both grids conform in all three directions. In the streamwise direction, cells are clustered at the rounded impingement edge with Δx =0.0023D and towards the outflow plane Δx =0.007D. In the spanwise direction, an equidistant grid with Δy =0.025D is used. In wall normal direction, a strong clustering at z=0 for the wall and shear layer with $\Delta z_{\min}$ =0.002D.

4. Results

In this section, we present profiles of time and spatially averaged velocity profiles at locations of interest indicated in Fig.2.
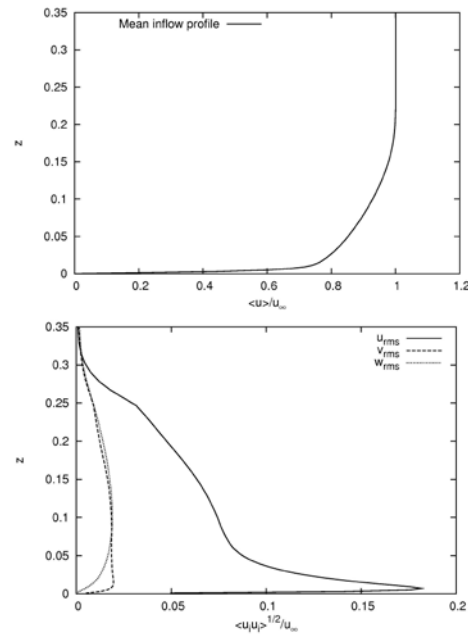
Fig 3: Mean inflow profile (top) imposing at the inlet (x=-2.85D) and the resulting fluctuations shown in r.m.s. of the velocities (bottom).

The averaging has been done over a time span of $200\, D/\mathrm{u}_\infty$ and in the spanwise direction. Our focus here lies on the description of the vortex inside the cavity, the boundary layer along the cavity's wall and the shear layer bounding the cavity.

4.1 Time-averaged quantities: profiles

The time-averaged tangential velocity profiles inside the cavity along the lines EF and AB are shown in Fig.4. In the centre of the cavity, the profiles are nearly straight lines which implies a solid-body rotation in this region whose coordinate $[x_c, z_c]$ = [0.18D,-0.44D] close to the center of the cavity. The radius $r = \sqrt{(x-x_c)^2 + (y-y_c)^2}$ is used when the positioning is referred to this center. The diameter of this is region is roughly 0.5D. The center can be identified by the inflection point of the gradient of the tangential velocity (not shown). Interestingly, the inner core region ($|r| \le$ 0.25D) rotates faster

than the outer part of the core ($0.2D \leq |r| \leq 0.5D$). This solid body rotation is enclosed by a boundary-layer-like region. The characteristics of this region are continuously changing along the curvature of the cavity. At **B**, the profile of the tangential velocity (Fig.4b) shows an inflection point which has visually disappeared at **E** (Fig.4a). This region is developed into a constant gradient at A (leeward side of the cavity) and later merged with the oncoming shear layer at the top of the cavity.

The wall-normal velocity shows a different direction of the fluids relative to the core. In Fig.4c the fluids is strongly moving from **B** towards the core and then decelerated once it reaches the core. Along **EF**, the fluid moves towards the wall in the boundary layer region and it travels to the shear layer across the core. Along **AB**, outside the boundary-layer-like region, there is relatively no radial motion of the fluid.

In what follows, we consider the Reynolds stresses on the same lines as the mean velocities. Note, that at line **AB**, the w_{rms} is in the streamwise direction of the local flow direction. We check if these values of the Reynolds normal stress could fit to the boundary layer along the cavity's wall. From Fig.4b, we learn that at point B the local free stream velocity, $u_1 \approx 0.25 u_\infty$. Based on this velocity, the corresponding peak of the r.m.s. of the fluctuations according to Fig.5a are approximately $0.25 u_l$, $0.24 u_l$ and $0.19 u_l$, in local streamwise, spanwise and normal direction, which is much larger than what can be observed in canonical boundary layers. In addition, the local boundary layer thickness is smaller than 0.05D. However, the extensions of the R.M.S. at point **B**

are approximately four times larger. At point **E**, we observe that the level of the normal stresses of the tangential component is slightly decreased while that of the wall-normal and the spanwise component are significantly reduced and they are still extending far more away from the wall than the local boundary layer thickness. At point **A**, the turbulence levels of the wall-normal and the spanwise velocities have only a half of their energy at **B**. Nevertheless, the turbulence intensity is way too strong to stem from a canonical boundary layer. This behaviour of the Reynolds normal stresses is far from that of a canonical zero pressure gradient boundary layer along the cavity wall --- with all consequences for modelling.

The Reynolds shear stress <u'w'> is plotted along lines **AB** and **EF** in Fig.5d&c. The shear stress behaves in a complicated way. First, it can be stated that is nearly symmetric on line AB with respect to the centre of the cavity with nine relative extrema. The first extrema is the center of the rotation. The next two extrema are the transition between the core and the boundary layer. At point B, we observe two local extrema that could correspond to the shear stress produced within the boundary layer along the cavity's wall. This suggests existence of back flow under the shoulder cavity, because it has the right sign and approximately the right position within the boundary layer thickness. When moving further to point E, the peak near the cavity's wall is still having the same strength while the second peak has disappeared. The near wall peak has the right sign to be able to stem from production within the boundary layer and has also the right extension. From this development one could

argue that the boundary layer along the cavity produces a reasonable shear stress. If that was true and would continue downstream of the boundary layer along the cavity's wall, then at point A, we would expect a negative <u'w'>, since the main production term in the balance equation for u'w' is negative $P_{13}=-<u'w'> \partial w / \partial x < 0$. The result shown in Fig.5c confirms this expectation.
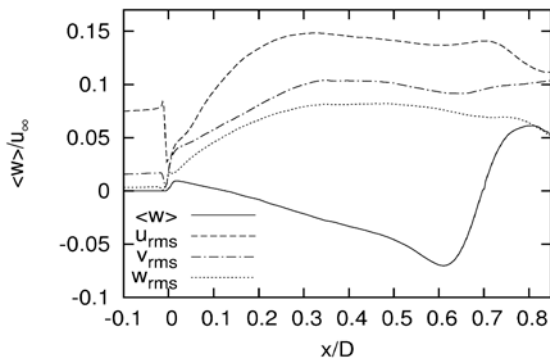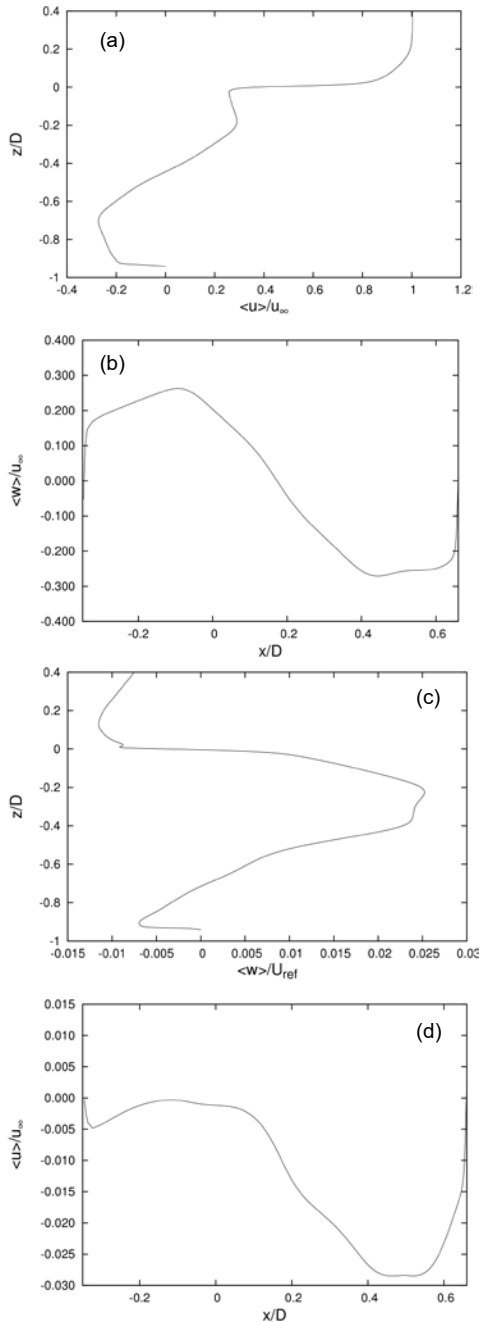

Fig. 6: Time-averaged wall-normal velocity (<w>) and Reynolds normal stresses along **DG**.

Next, we concentrate on the development of the shear layer bounding the cavity along line *DG*. This shear layer drives the vortex inside the cavity by exchanging momentum by viscous and, *more importantly*, *the turbulent stresses*. In Fig.5c we plotted already the turbulent shear stress <*u*'w'> at two streamwise positions within the shear layer. Directly at the cusp above the cavity (*z* > 0), there is the shear stress profile coming from the boundary layer upstream which has negative sign and a thin positive peak of <*u*'w'> just beneath the cusp coming from the cavity. At 0.18*D* downstream, the thin shear layer has produced a second peak with negative <*u*'w'> which is much stronger than the two peaks that are observable at the separation from the cusp. The instabilities within the shear layer are excited very fast which is certainly the result of the

returning turbulence convected by the vortex inside the cavity. The streamwise developments of the wall normal velocity component and the Reynolds normal stresses are plotted in Fig.6. Just after the cusp, the normal component is positive as a consequence of the finite angle of the cusp. As the shear layer widens, the normal velocity turns its sign and transports fluid towards the cavity. As the impingement edge is approached it changes sign again which can be the result of the fluid moving away from the stagnation point. The normal Reynolds stresses undergo a fast transition towards a plateau that lasts until the region over the impingement edge is reached. The velocity difference in the shear layer could be estimated as large as approximately $u_s = 0.7 u_\infty$. With that in mind, one would expect from plane mixing layer the R.M.S. in the range of $0.12 u_\infty$, $0.10 u_\infty$ and $0.08 u_\infty$ for the streamwise, the spanwise and the wall-normal velocity, respectively. The R.M.S values are close to this expectation. This development of the boundary layer into a plane-mixing layer only takes $1.5 \delta_0$, the boundary layer thickness at the cusp. This plane mixing layer is disrupted after the peak of the wall-normal velocity which is close to the shoulder of the cavity.

Due to limited space, the flow mechanism is summarized as follows. The flow can be divided into three zones namely; (i) shear layer, (ii) stagnation point, (iii) vortex core and (iv) boundary layer along the cavity wall. The *shear layer (i)* above the cavity is a highly active region that is excited by both, the turbulent boundary layer coming from upstream and the fluctuations coming from inside the cavity. The fluctuations reach approximately standard values of a mixing

layer after a strong amplification immediately after separation from the cusp of the cavity. The low pressure in the shear layer entrains fluid from inside the cavity and thus contributes to the rotational motion of the vortex cell whose central (iii) part is almost a solid body rotation in the mean.


Fig 4: Time-averaged profile inside the cavity: tangential velocity along **EF** (a) and **AB** (b), wall-normal velocity along **EF** (c) and **AB** (d).
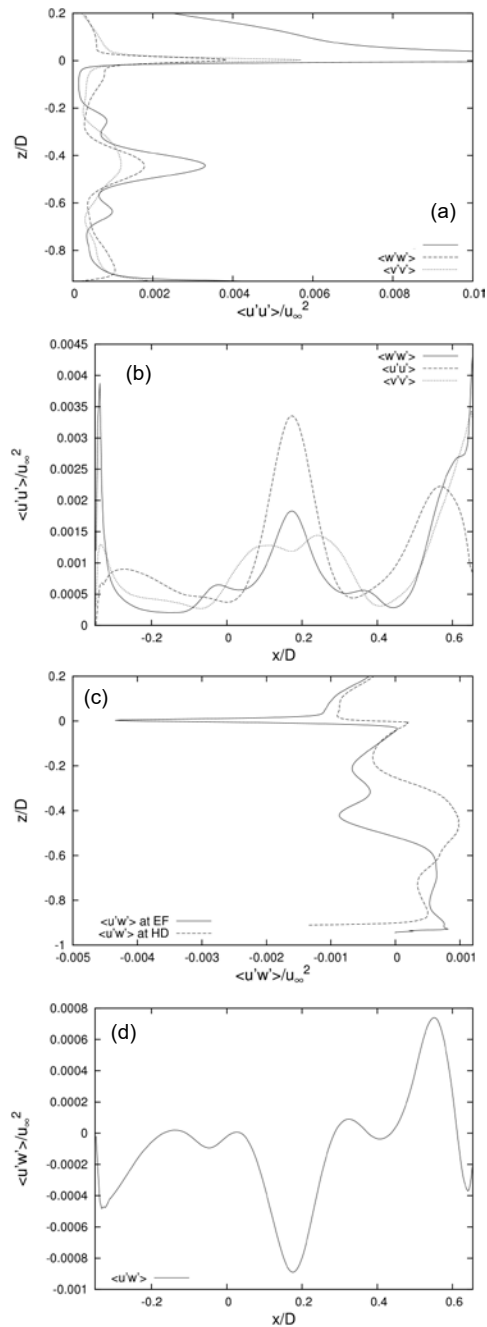
Fig 5: Reynolds stresses inside the cavity: normal stresses at **EF** (a) and **AB** (b) and shear stresses at **EF** (c) and **AB** (d).

The stagnation point (ii) generates turbulent kinetic energy (Fig.7) and drives high-energy packets of fluid into the cavity which seems to be responsible for the largest contribution to the rotational motion in the core. These energy packets are forming the boundary layer (iv) along

the cavity's wall, even though its characteristics are not yet reach those of the canonical one.
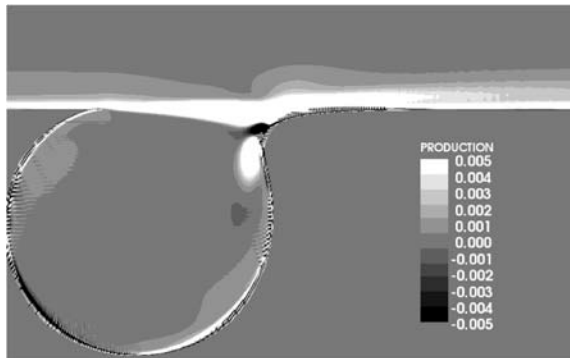
Fig 7: Spatial distribution of the production of turbulent kinetic energy.

6. Acknowledgement

7. References

[1] J. H.Ferziger and M. Peric. *Computational Methods for Fluid Dynamics*. Springer, 1996.

[2] F. Tremblay. Direct and large-eddy simulation of flow around a circular cylinder at sub-critical Reynolds numbers Dissertation, Technische Universitaet Muenchen, Fakultaet fuer Maschinenwesen, 2002

[3] F. Tremblay, M. Manhart, and R. Friedrich. DNS and LES of flow around a circular cylinder at a subcritical Reynolds number with Cartesian grids. In R. Friedrich and W. Rodi, editors, *LES of complex transitional and turbulent flows*, p.133-150, Dordrecht, 2001. Kluwer Academic Publishers.

[4] M. Manhart, F. Tremblay, and R. Friedrich. MGLET: a parallel code for efficient DNS and LES of complex geometries. In Jensen et al., editor, *Parallel Computational Fluid Dynamics 2000*, p.449-456, Amsterdam, 2001. Elsevier Science B.V.

[5] M. Manhart. A zonal grid algorithm for DNS of turbulent boundary layers. *Computers & FLuids*, 33(3):435–461, 2004.

[6] N. Peller, A. Le Duc, F. Tremblay, and M. Manhart. High-order stable interpolations for immersed boundary methods. *International Journal for Numerical Methods in Fluids.*, 52(11):1175-1193, 2006

[7] J. Gradl, H. Schwarzer, F. Schwertfirm, M. Manhart, W. Peuker. Coupling the particle population dynamics with hydrodynamics through direct numerical simulation *Chemical Engineering and Processing* 45(10): 908–916, 2005.

[8] S. Eisenbach, R. Friedrich. Large-eddy simulation of flow separation on an airfoil at a high angle of attack and Re=105 using Cartesian grids *Theoretical and Computational Fluid Dynamics* 22(3):213–225, 2008.

[9] H. A. Khaledi, V D. Narasimhamurthy, and H. I. Andersson. Cellular vortex shedding in the wake of a tapered plate at low Reynolds number *Phys. Fluids* 21(1):013603, 2009.

[10] C. Meneveau, T. S. Lund and W. H. Cabot. A Lagrangian dynamic subgrid-scale model of turbulence. *Journal of Fluid Mechanics.*, 319:353-385, 1996.

[11] P. R. Spalart. Direct simulation of a turbulent boundary layer up to R_- = 1410. *Journal of Fluid Mechanics.*, 187:61-98, 1988.

[12] M. Manhart and R. Friedrich. DNS of a turbulent boundary layer with separation. Int. J. Heat and Fluid Flow, 23(5):572-581, 2002.

[13] T. S. Lund, X.Wu and K. D. Squires. Generation of Turbulent Inflow Data for Spatially-Developing Boundary Layer Simulations. *Journal of Computational Physics*, 140:223- 258, 1998.